Soft-x-ray polarimeter with multilayer optics: complete analysis of the polarization state of light

Franz Schäfers, Hans-Christoph Mertins, Andreas Gaupp, Wolfgang Gudat, Marcel Mertin, Ingo Packe, Frank Schmolla, Silvia Di Fonzo, Gérard Soullié, Werner Jark, Richard Walker, Xavier Le Cann, Ralf Nyholm, and Mikael Eriksson

The design of a versatile high-precision eight-axis ultrahigh-vacuum-compatible polarimeter is presented. This multipurpose instrument can be used as a self-calibrating polarization detector for linearly and circularly polarized UV and soft-x-ray light. It can also be used for the characterization of reflection or transmission properties (reflectometer) or polarizing and phase-retarding properties (ellipsometer) of any optical element. The polarization properties of Mo/Si, Cr/C, Cr/Sc, and Ni/Ti multilayers used in this polarimeter as polarizers in transmission and as analyzers in reflection have been investigated theoretically and experimentally. In the soft-x-ray range, close to the $2p$ edges of Sc, Ti, and Cr, resonantly enhanced phase retardation of the transmission polarizers of as much as 18° has been measured. With these newly developed optical elements the complete polarization analysis of soft-x-ray synchrotron radiation can be extended to the water-window range from 300 to 600 eV.

OCIS codes: 120.2130, 340.6720, 340.7480, 120.7000, 120.5700, 230.5440.

1. Introduction

Circularly polarized synchrotron radiation has attracted growing interest at various synchrotron radiation centers for the study of a wide range of phenomena in biology, chemistry, physics, and material science. Special insertion devices have been proposed and fabricated that produce predominantly elliptically or circularly polarized light.[1–4]

Circularly polarized light in the vacuum-ultraviolet (VUV) and soft-x-ray ranges is of particular interest for the investigation of the $2p$ absorption edges of the magnetic metals Fe, Co, and Ni and the $3d$ absorption edges of the rare-earth elements.[5,6] Such experiments are important, e.g., for the development of ultrafast, high-capacity magneto-optical memory. The availability of circularly polarized light has stimulated novel types of experiments, e.g., in spinresolved photoemission and Auger emission[7]; circular dichroism on magnetic, nonmagnetic, and chiral materials; and magnetic microscopy.[8,9] Valuable information can be obtained, e.g., about the structure of organic chiral molecules, i.e., those that exist in both right-handed and left-handed symmetry.[10] Scattering of circularly polarized radiation provides structural information about the helical organization of complex biological structures such as proteins, nucleic acids, and viruses. For a quantitative understanding of the underlying physical processes, however, the knowledge of the polarization state is necessary, because these effects are proportional to the degree of circular polarization. As only a few optical elements for polarization analysis have been produced so far, the exact polarization state of the light in this energy range is rarely known precisely.

Polarization can be described in terms of a four-component (S_0, S_1, S_2, and S_3) Stokes vector that determines the total intensity (S_0), the linear intensity (S_1, S_2), and the circularly polarized intensity (S_3).[11] Elliptically polarized light is a mixture of S_1, S_2, and S_3. To make a complete polarization analysis of light, one needs both a polarizer (preferably a quarter-wave plate) to introduce phase retardation between the two electric-field components and an an-

F. Schäfers, H.-C. Mertins (mertins@exp.bessy.de), A. Gaupp, W. Gudat, M. Mertin, I. Packe, and F. Schmolla are with Bessy Electronenspeicherring-Gesellschaft fur Synchrotronstrahlung mbH, Lentzeallee 100, D-14195 Berlin. S. Di Fonzo, G. Soullié, W. Jark, and R. Walker are with Sincrotrone Trieste, S.S. 14, KM 163.5 in Area Science Park, I-34012 Basovizza, Italy. X. Le Cann, R. Nyholm, and M. Eriksson are with MAX-Laboratory, Lund, Sweden.

Received 4 January 1999; revised manuscript received 29 March 1999.

0003-6935/99/194074-15$15.00/0

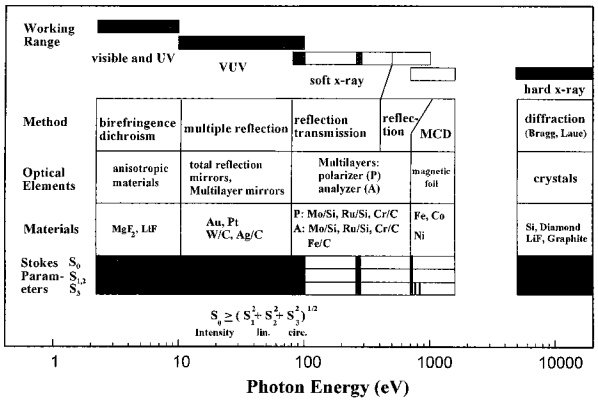

Fig. 1. Methods for polarization analysis from the visible to the x-ray ranges. The working ranges, methods, optical elements, and the obtainable polarization data in terms of Stokes parameters are indicated (see text for references).

alyzer that transmits preferably only one particular linearly polarized component. A polarization measurement requires independent rotations of these two optical components about the optical axis while the transmitted intensity is recorded. A fit to the transmitted intensity then gives the normalized Stokes parameters as well as the polarizing properties of the optical elements used, i.e., the phase retardation and the transmission and reflection ratios for *s*- and *p*-polarization geometry.[12,13]

A survey of the methods used for polarization analysis in energy ranges from the visible to the x-ray regions of the electromagnetic spectrum is given in Fig. 1. Commercially available detectors exist for the visible and the near UV that exploit the birefringence or dichroism of anisotropic materials such as MgF_2 and LiF crystals.[14,15] In the VUV, where no transparent materials exist, multiple-reflection mirror systems consisting of three or four mirrors are used[16–18] whose incidence angles and coatings are optimized for optimum polarizer or analyzer behavior.

At energies above approximately 100 eV this technique is not applicable because the reflectance at the large incidence angles needed is too poor. Reflection mirrors with and without multilayers at incidence angles close to the Brewster's angle of approximately 45° for use as Rabinovitch detectors for the determination of linear polarization are common in the soft-x-ray range.[18–22]

Above 2.5 keV, diffraction on Si, diamond, or graphite single crystals in Bragg or Laue geometry is applied to generate broadband quarter-wave phase plates for the analysis or the generation of circular polarization.[23–27]

The energy range above 700 eV can be covered by magnetic foils or multilayers. In this range, magnetic circular dichroism (MCD) and the Faraday effect at the 2*p* absorption edges of the transition materials and at the 3*d* edge of rare earths are starting to be used for quantitative determination of the degree of circular polarization.[28,29]

For the soft-x-ray range the use of multilayers working in transmission as phase retarders has been suggested.[30,31] Only two operating systems, however, have been reported: With Mo/Si a quarter-wave plate was realized for energies below the Si 2*p* edge.[32–34] This system is now routinely used also for the conversion of linearly into circularly polarized light.[35] With a Cr/C multilayer a considerably smaller phase retardation of 5° was achieved at the C 1*s* edge, which, however, was sufficient for the analysis of circular polarization.[36,37] For higher photon energies multilayer systems based on Ni/Sc, Ni/BN, and Ni/V have been suggested to work at the 2*p* absorption edges of the respective materials Sc and V.[38] Recently new transmission and reflection multilayers for this water-window energy range were successfully produced and tested,[39–42] but so far they have not been used for polarization measurements. A complete polarization measurement with optical standards was therefore limited to energies below the C 1*s* edge.

Various designs for VUV and soft-x-ray polarimeters compatible with ultrahigh-vacuum (UHV) conditions have been realised[18]: In a simple Rabinovitch detector only one reflection-type optical element needs to be rotated about the direction of the incident light, which will allow linear polarization measurements to be performed at an energy given by the reflection characteristics of the optics used.[21,22] By use of graded multilayers, one can extend the optics working range.[43] A complete polarization measurement employs independent azimuthal rotations of two optical elements at fixed incidence angles. Such devices were realized for three- and four-mirror systems[12,16,17] and for transmission polarizer optics by which the light direction is unchanged after the first reflection or transmission. The most flexibility is found in an ellipsometer system for transmission or reflection polarizers for which the analyzer section must be rotated about the polarizer.[34,44]

In this paper we present the design and performance of a novel high-precision eight-axis UHV-compatible polarimeter as well as experimental data on newly developed multilayer systems for polarization analysis in the soft-x-ray range. The new versatile chamber can be used for two purposes: the characterization of new optical elements (reflectometer–ellipsometer) and complete polarization analysis of soft-x-ray synchrotron radiation (polarimeter). A detailed description of the polarimeter is given in Section 3 below. In Section 2 we deal with the basic principles of polarimetry, the physics of linearly polarizing reflection multilayers, and phase-retarding transmission multilayers. In Section 4 the experimental data on reflection and phase retardation of the newly developed Mo/Si, Cr/C, Cr/Sc, and Ni/Ti multilayers are presented and discussed.

2. Theoretical Considerations

A. Polarimetry

For the description of polarized light the electrical field is separated into orthogonal components E_s and

E_p, that are perpendicular (E_s) and parallel (E_p) to the plane of incidence:

$$E_{s,p}(z, t) = E^0_{s,p}\exp[i(\omega t - kz + \varphi_{s,p})], \quad (1)$$

The field propagates in the z direction with frequency ω, time t, wave vector k, and phase $\varphi_{s,p}$. The interaction of light with an optical element is described by the complex coefficients of reflection $r_{s,p}$, transmission $t_{s,p}$, and induced phase shift $\delta_{s,p}$. Measurable quantities are reflectance $R_{s,p}$, transmittance $T_{s,p}$, and total phase retardation Δ, as given by

$$\begin{aligned} R_{s,p} &= r_{s,p}r_{s,p}^*, \qquad r_{s,p} = |r_{s,p}|\exp(i\delta_{s,p}), \\ T_{s,p} &= t_{s,p}t_{s,p}^*, \qquad t_{s,p} = |t_{s,p}|\exp(i\delta_{s,p}), \\ \Delta &= \delta_s - \delta_p. \end{aligned} \quad (2)$$

The polarization of the light is described by the Stokes vector $S = (S_0, S_1, S_2, S_3)$. The parameters S_0 (intensity), S_1 (linear polarisation), S_2 (linear polarisation in a plane rotated by 45° with respect to the S_1 plane), and S_3 (circular polarization) in terms of the electric-field components E_s and E_p are given by[13]

$$\begin{aligned} S_0 &= [(E_p^0)^2 + (E_s^0)^2]/2, \\ S_1 &= [(E_p^0)^2 - (E_s^0)^2]/2, \\ S_2 &= E_p^0 E_s^0 \cos(\varphi_p - \varphi_s), \\ S_3 &= -E_p^0 E_s^0 \sin(\varphi_p - \varphi_s). \end{aligned} \quad (3)$$

The total degree of polarization P is given by

$$P = [(S_1^2 + S_2^2 + S_3^2)/S_0^2]^{1/2} \le 1. \quad (4)$$

Experimental control of the polarization state of a photon beam can be obtained with appropriate optical elements optimized as phase retarders (polarizers) and analyzers (Fig. 2). The polarizer introduces phase retardation between the two orthogonal components (E_p, E_s) of the electric field, whereas the analyzer reflects preferentially one (E_s) of the two components. A polarization measurement requires independent rotation of both elements about the direction of light such that the polarization state is changed by the first and then analyzed by the second element.

The interaction of light with an optical element can be described by the Müller matrix M (Ref. 13):

$$M = \begin{bmatrix} 1 & -\cos 2\Psi & 0 & 0 \\ -\cos 2\Psi & 1 & 0 & 0 \\ 0 & 0 & \sin 2\Psi \cos(\delta_p - \delta_s) & \sin 2\Psi \sin(\delta_p - \delta_s) \\ 0 & 0 & -\sin 2\Psi \sin(\delta_p - \delta_s) & \sin 2\Psi \cos(\delta_p - \delta_s) \end{bmatrix}, \quad (5)$$

with $\tan\Psi = T_p/T_s$ (R_p/R_s) for transmitting (reflecting) optics and the phase retardation $\delta_p - \delta_s$ induced by the optics. The Müller matrix reduces to simpler cases for an ideal phase retarder, namely, a quarter-wave plate, for which $\Delta = 90°$ and $2\Psi = 90°$, corresponding to $T_s = T_p$. Similarly, for an ideal analyzer R_p will be zero, corresponding to $\Psi = 0°$, and no further phase retardation will be induced ($\Delta = 0°$).

As sketched in Fig. 2, the Stokes vector, a set of real quantities with dimensions of intensities, can be measured by independent rotation of the polarizer and analyzer–detector assembly about the optical axis, i.e., about α and β, respectively. These azimuthal rotations correspond to a coordinate transformation given by the rotation matrix

$$R(\alpha, \beta) = \begin{bmatrix} 1 & 0 & 0 & 0 \\ 0 & \cos 2(\alpha, \beta) & \sin 2(\alpha, \beta) & 0 \\ 0 & -\sin 2(\alpha, \beta) & \cos 2(\alpha, \beta) & 0 \\ 0 & 0 & 0 & 1 \end{bmatrix}. \quad (6)$$

After the light has passed through both optical elements, its polarization is described by Stokes vector S_f, which is a product of the Stokes vector of incident light S_i, the Müller matrices M_1 (polarizer) and M_2 (analyzer), and the rotation matrices $R(\alpha)$ and $R(\beta)$:

$$\mathbf{S}_f = R(-\beta)M_2R(\beta)R(-\alpha)M_1R(\alpha)\mathbf{S}_i. \quad (7)$$

The transmitted intensity S_{f0} that is measured with the detector is given by[12]

$$\begin{aligned} S_{f0}(\alpha, \beta) = {} & \tfrac{1}{2}(T_s + T_p)\tfrac{1}{2}(R_s + R_p)\{S_0 \\ & + \cos 2\alpha(-S_1 \cos 2\psi_1) + \sin 2\alpha(-S_2 \cos 2\psi_1) \\ & + \cos 2\beta[-S_1 \cos 2\psi_2 \tfrac{1}{2}(1 + \sin 2\psi_1 \cos\Delta_1)] \\ & + \sin 2\beta[-S_2 \cos 2\psi_2 \tfrac{1}{2}(1 + \sin 2\psi_1 \cos\Delta_1)] \\ & + \cos 2\alpha \cos 2\beta[+S_0 \cos 2\psi_1 \cos 2\psi_2] \\ & + \sin 2\alpha \cos 2\beta[+S_3 \sin 2\psi_1 \cos 2\psi_2 \sin\Delta_1] \\ & + \cos 2\alpha \sin 2\beta[-S_3 \sin 2\psi_1 \cos 2\psi_2 \sin\Delta_1] \end{aligned}$$

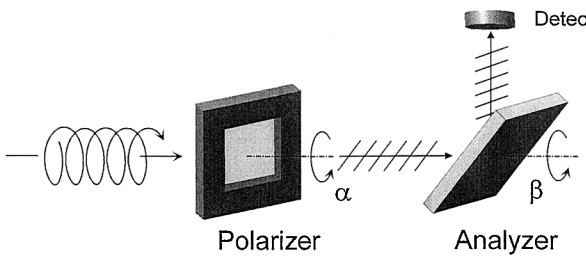

Fig. 2. Schematic setup for polarization measurement with optical standards: a transmission polarizer and a reflection analyzer. Both elements are rotated independently about the beam axis (α and β, respectively) while the transmitted intensity is measured with the detector.

$$+ \sin 2\alpha \sin 2\beta[+S_0 \cos 2\psi_1 \cos 2\psi_2]$$

$$+ \cos 4\alpha \cos 2\beta[-S_1 \cos 2\psi_2 \tfrac{1}{2}(1 - \sin 2\psi_1 \cos \Delta_1)]$$

$$+ \sin 4\alpha \cos 2\beta[-S_2 \cos 2\psi_2 \tfrac{1}{2}(1 - \sin 2\psi_1 \cos \Delta_1)]$$

$$+ \cos 4\alpha \sin 2\beta[+S_2 \cos 2\psi_2 \tfrac{1}{2}(1 - \sin 2\psi_1 \cos \Delta_1)]$$

$$+ \sin 4\alpha \sin 2\beta[-S_1 \cos 2\psi_2 \tfrac{1}{2}(1 - \sin 2\psi_1 \cos \Delta_1)]\}. \quad (8)$$

Equation (8) includes as unknowns the Stokes vector of the incident light to be determined (S_0, S_1, S_2, S_3) as well as the phase-shifting and polarizing properties of the two optical elements: $\Delta_1 = \delta_p - \delta_s$, $T_p/T_s = \tan \Psi_1$, and $R_p/R_s = \tan\Psi_2$. Note that Δ_2, the phase retardation of the analyzer, does not come into effect as long as the detector response is polarization insensitive.

By a least-squares fit to the measured data these seven unknowns can finally be determined. Thus this measurement is a self-calibrating procedure that facilitates both the characterization of the incident light and determination of the polarizing properties of the two optical elements used.

B. Reflection Analyzer

In the soft-x-ray range, multilayers are the appropriate polarizing optical elements to be used as reflection analyzers.[31] For this purpose they must be optimized with respect to a large reflectance R_s and a large suppression ratio linear polarizing power R_s/R_p. Both conditions can be fulfilled at the Brewster's angle, which in the soft-x-ray range is close to 45°. In Fig. 3 the maximum theoretical reflectance at angles close to the Brewster's angle is plotted for a variety of multilayer systems. These calculations are based on the Fresnel equations for which the computer program REFLEC (Ref. 45) and the optical constants derived by Henke *et al.*[46] are used. For the calculation the d spacing was varied with the photon wavelength λ according to $d = \lambda/[2\sin(45°)]$, including refraction correction and assuming no interface roughness ($\sigma = 0$) and 0.3 nm (dotted curves), 200 periods, and a thickness ratio $\gamma = d_A/(d_A + d_B) = 0.4$ ($d_{A,B}$ are layer thicknesses of the absorber and the spacer, respectively). All samples show a resonantly enhanced reflectance at an absorption edge of one of the materials with peak values from 60% to 80% at the Si 2*p* (99 eV), C 1*s* (284 eV), Sc 2*p* (399 eV), Ti 2*p* (454 eV), and V 2*p* (512 eV) edges. All multilayers can be operated in two working ranges, namely, at the absorption edges of the spacer and the absorber materials. In the low-energy range from 50 to 512 eV the multilayers cover a fairly large energy range below the edge with slightly reduced performance, so this range, in particular the water-window region from 280 to 540 eV, can be covered with a few multilayer systems with peak reflectances higher than 20%. However, above 512 eV, multilayers that contain Cr, Fe, and Ni show good performance only close to the 2*p* absorption edges.

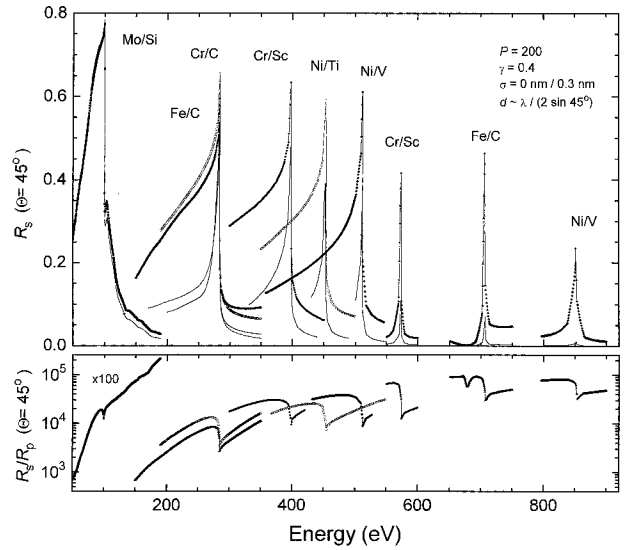

Fig. 3. Top, Calculated peak reflectance data (R_s at 45°) for ideal multilayer structures without roughness [$\sigma = 0$ nm (symbols)] and for $\sigma = 0.3$ nm, (dotted curves). The period is matched to the photon wavelength according to $d = \lambda/2 \sin(45°)$ including refraction corrections. Best performance is obtained at and below the respective absorption edges. Bottom, corresponding theoretical linear polarizing power R_s/R_p at 45° of the same multilayer structures.

In Fig. 3 (bottom) the corresponding suppression ratio R_s/R_p is plotted for the same multilayers for a fixed incidence angle of 45°. The linear polarizing power increases with higher energy because then the Brewster's angle approaches 45° and thus R_p gets increasingly more suppressed. Immediately beside an absorption edge R_s/R_p has a minimum that is due to the resonance behavior of R_s. Note that in practice R_s/R_p may be considerably smaller because of the energy bandwidth and the finite angular spread (divergence) of the incident light, a factor that is not taken into account in the calculations shown here. This sensitivity to the angle of incidence can be seen in Fig. 4.

Figure 4 shows the dependence of R_s, R_p, and R_s/R_p on the angle of incidence for a fixed energy, calculated for two Cr/Sc systems of slightly different periods d. The $d = 2.21$ nm sample (Fig. 4, left) is matched to $\theta = 45°$, the Brewster's angle; thus both linear polarizing power and reflectance are maximum at this angle. When the period ($d = 2.14$) is not exactly matched to 45° (Fig. 4, right), the Bragg angle ($\theta_{\text{Bragg}} = 47°$) moves away from the Brewster's angle. Consequently R_s/R_p is considerably smaller at θ_{Bragg} because then R_p is no longer suppressed completely. This case is the more realistic one in polarimetry applications in which only one optical element is used in an energy range about the optimal energy. For maximum reflectance the multilayer is always operated at the Bragg angle, with the consequence that R_s/R_p can be reduced. To avoid this problem one can use graded multilayers with tunable periods to cover the energy range of interest.[43] One should notice that the large theoretical linear polarizing power,

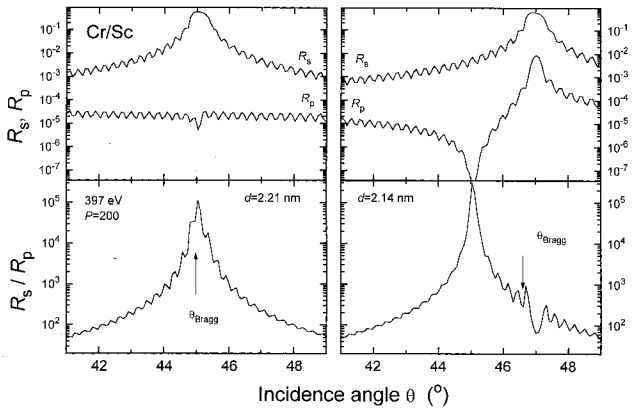

Fig. 4. Reflectances R_s, R_p and linear polarizing power R_s/R_p at 397 eV as functions of the incidence angle calculated for two Cr/Sc multilayers with slightly different periods d. Left, period matched to the Brewster's angle, coincidence of Bragg reflection peak and maximum linear polarizing power. Right, mismatch of Bragg and Brewster's angles.

of the order of 10^5, is predominantly an effect of the singularity in R_p at the Brewster's angle. A detailed discussion of the angular and energy dependence of the experimental linear polarizing power data is given in Subsection 4.B below.

C. Phase Retarder

Multilayers operated in transmission close to the Bragg angle introduce a phase retardation Δ between the transmitted s and p components of the electrical field.[30] For the special case of $\Delta = 90°$ linearly polarized light can be completely converted into circularly polarized light and vice versa. This effect is comparable with the birefringence of a uniaxial crystal, which is explained by the two different refractive indices n_o and n_{eo} for the ordinary and the extraordinary beams, respectively. In this case the two different phase velocities c/n_o and c/n_{eo} for the two polarization directions parallel and perpendicular to the optical axis lead to a phase retardation Δ that is proportional to $n_o - n_{eo}$.[11]

The geometry associated with transmission multilayers is depicted in Fig. 5 for the azimuthal angle $\alpha = 45°$ ($|E_s| = |E_p|$) for linearly polarized light. The optical axis is given by the surface normal, i.e., the growth direction of the layers. Incident field component E_s oscillates within the plane of the interfaces; E_p is projected into a component parallel (E_{pp}) or perpendicular (E_{ps}) to the surface normal. These components ($E_s + E_{ps}$ and E_{pp}) accelerate the electrical charges with different amplitudes. This asymmetry is expressed by the different polarizabilities described by a dielectric tensor ϵ and results in refractive indices $n_o = \sqrt{\epsilon_o}$ and $n_{eo} = \sqrt{\epsilon_{eo}}$ with different phase velocities for the two field components, leading to small phase shifts δ_s and δ_p at each interface. This asymmetry vanishes for normal incidence ($\Theta = 90°$) and increases with smaller Θ. An enhancement of this effect is achieved in the Bragg condition, when standing waves are induced, of which

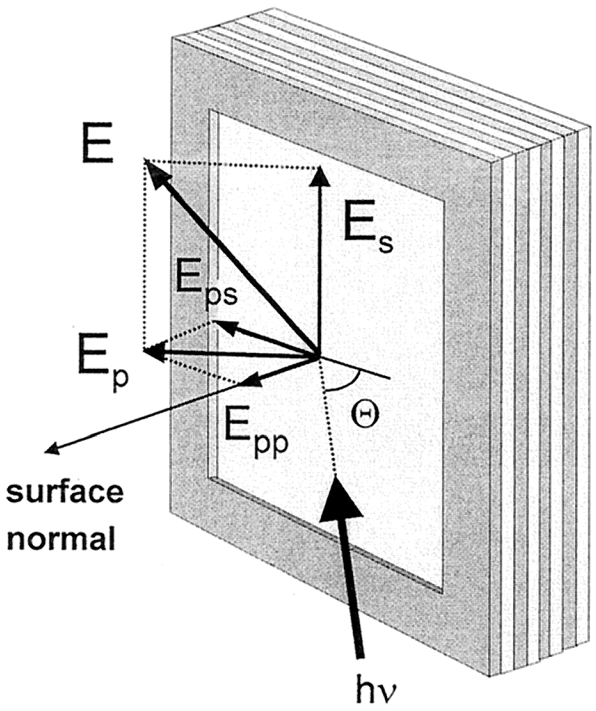

Fig. 5. Geometry of phase-retarding transmission multilayers: The electric-field components E_s and E_p are projected perpendicularly (E_{ps} and E_s) and parallel (E_{pp}) to the surface normal.

the maximum intensity $|E_s + E_{ps}|^2$ is centered in the spacer ($\Theta < \Theta_{Bragg}$) or in the absorber material ($\Theta > \Theta_{Bragg}$).[47] E_{pp}, and thus also δ_p, is not affected by the resonance. Thus E_s is retarded ($\Theta < \Theta_{Bragg}$) or advanced ($\Theta > \Theta_{Bragg}$) with respect to E_p. The phases can be deduced from Eq. (1) (Ref. 11):

$$\delta_{s,p} = \tan^{-1}(\mathrm{Im}[E_{s,p}]/\mathrm{Re}[E_{s,p}]). \quad (9)$$

As for a $\lambda/4$ plate, the phase retardation introduced depends on the azimuth α with maximum Δ for $\alpha = 45° \pm n\pi/2$ ($n = 0, 1, 2 \ldots$).

As an example, this phase retardation is plotted in Fig. 6 for Cr/Sc ($d = 2.44$ nm) for a photon energy of 397 eV immediately below the Sc $2p$ edge. The Bragg reflection peak will appear at an incidence angle of 40°. This peak is connected with a minimum in transmission (Fig. 6, top), which is more pronounced in s- than in p-polarization geometry. The relative phase $\Delta = \delta_s - \delta_p$, plotted in the lower part of Fig. 6, is negative at angles smaller than θ_{Bragg} and positive at larger angles. At θ_{Bragg}, Δ changes sign. The phase retardation increases with the number of contributing layers.

The dependence of phase retardation Δ on the period thickness of a multilayer is plotted in Fig. 7 (top). Calculations were performed for Cr/Sc at 397 eV. According to the Bragg equation, the Bragg (reflection or transmission) resonance associated with resonance in Δ appears at different angles of incidence of 10°–67°. In normal incidence ($\theta = 90°$) both E_p and E_s are perpendicular to the surface normal; with smaller angles the field component E_{pp} parallel to the

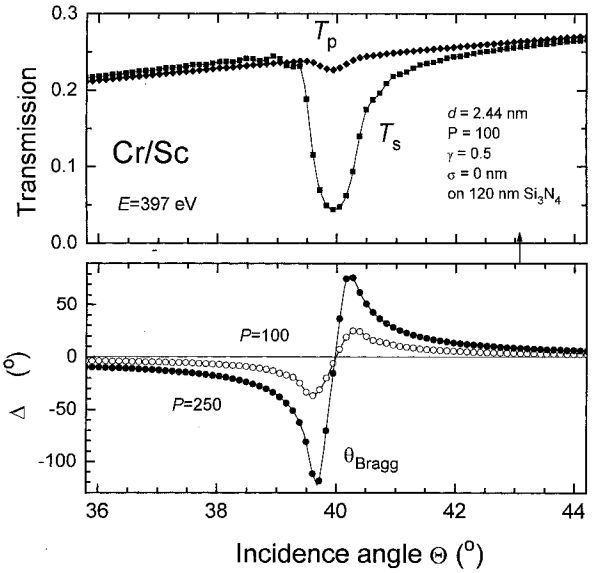

Fig. 6. Transmission and phase retardation (Δ) for a Cr/Sc transmission multilayer in the vicinity of the Bragg angle calculated for 397 eV, close to the Sc 2*p* absorption edge.

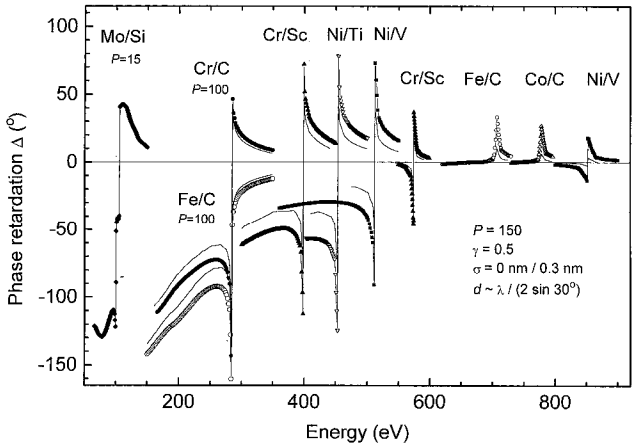

Fig. 8. Phase-retarding transmission multilayers for the soft x-ray region. The maximum achieveable phase retardation Δ was calculated for ideal structures without roughness [(σ = 0 nm (symbols)] and for σ = 0.3 nm (dotted curves), at the angle of optimum figure of merit (θ ≈ 30°). The period thickness is matched to the photon wavelength according to $d = \lambda/2 \sin(30°)$, including reflection corrections.

surface normal (Fig. 5) increases. Consequently the phase retardation, which is zero for θ = 90°, increases with smaller angles. Thus according to this behavior the optimum phase-retarding multilayer would require the largest thickness compatible with the Bragg equation for the desired photon energy and would operate at the smallest possible incidence angle, which, however, will be well above the total reflection regime (θ < 4°) because of the vanishing transmission. For some asymmetric crystals, calculations predict a large phase retardation for applications in the total-reflection mode.[48]

For practical applications the figure of merit for phase-retarding transmission elements is given by the product of the transmittance and the sine of the phase retardation, which is a measure of its circular polarizing power.[31] This figure of merit is shown in Fig. 7 (bottom). Because the effective thickness scales with 1/sin θ and thus the transmission behavior is opposite that of the phase retardation, the optimum angle turns out to be approximately 30°, which for this multilayer corresponds to a period of $d = 3.12$ nm. This optimum is, however, independent of energy and material, because the optimum figure of merit is a result of pure geometrical considerations.

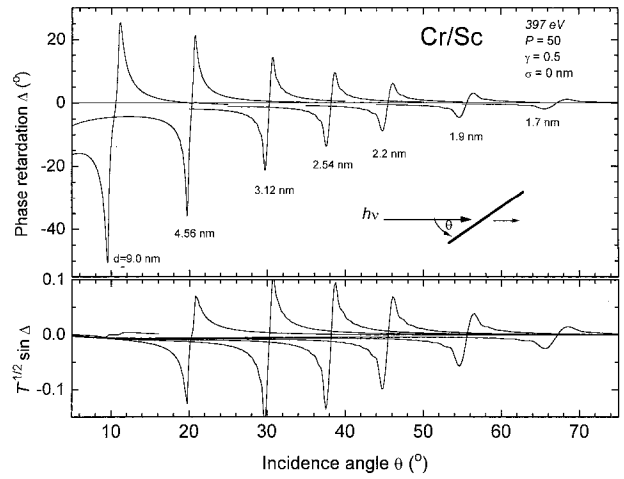

Fig. 7. Phase retardation and figure of merit ($T^{1/2}$ sin Δ) for Cr/Sc transmission multilayers of different period thicknesses in the vicinity of the Bragg angle calculated for 397 eV.

The selection of the optimum material combination for phase-retarding transmission multilayers is made by the same optimization procedure as described in Subsection 2.B for reflection multilayers with special emphasis on highly transparent materials. Figure 8 gives a theoretical survey of promising material combinations, benefitting predominantly from the pronounced 2*p*–3*d* resonances of 3*d* transition metals for the water-window range. We performed the calculations by varying the period with the wavelength according to $d = \lambda/2 \sin(30°)$ including refraction corrections, to stay at the best figure of merit ($T^{1/2}$ sin Δ). We iteratively found the maximum achievable Δ by changing the incidence angle near 30°. The absorption edges clearly appear as pronounced resonances in the phase retardation for all samples. At the resonance energy the sign changes from negative to positive. Above the absorption edge a large phase retardation is observed, but the figure of merit is poor because of the low transmission. For the highest energies in Fig. 8 period *d* gets as small as 1.45 nm (Ni/V). Such multilayers have, however, been successfully realized,[40] thus making phase retarders for these energies possible. Roughness, however, seriously degrades the remaining phase retardation (dotted curves).

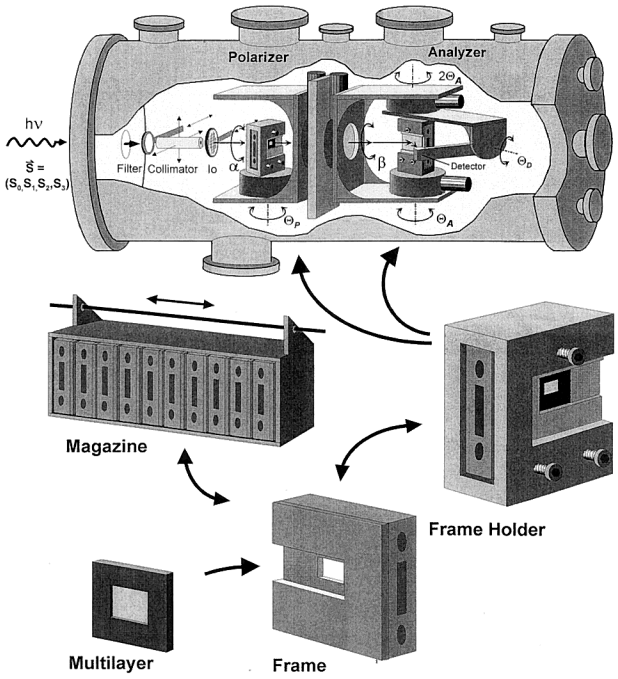

Fig. 9. Schematic view of the soft-x-ray polarimeter, Multilayer, frame, magazine store, and frame holder are shown separately.

Table 1. Applications and Technical Features of the Soft-X-Ray Polarimeter

Application and their features
Determination of Polarization (Stokes)
S_0 (intensity); S_1, S_2, (linear), S_3 (circular)
Optical elements
Polarizer: transmission multilayer, $\lambda/4$ plates (MgF_2)
Analyzer, reflection multilayer (Mo/Si, Cr/C, Cr/Sc, Ni/Ti)
Working energy
Visible to soft-X-ray, determined by optical elements in use
Characterization of optical elements
Multilayers, transmission foils, crystals: reflectance, transmission, phase retardation, s- and p-polarization geometry
Technical features
Eight-axis polarimeter
Collimator (pinholes ∅: 0.2–2 mm), translation in x, y ± 12 mm
Polarizer–analyzer: azimuthal angle, $0° \le \alpha, \beta \le 370°$; incidence angle, $0° \le \Theta_P, \Theta_A \le 90°$
Detector (GaAsP diode): scan range, in-plane $0° \le 2\Theta_A \le 180°$, off-plane $\Theta_D \le \pm 27°$
UHV Compatible, $p \le 1 \times 10^{-6}$ Pa
UHV goniometers, motors for positioning: increment 0.001°, accuracy 0.01°
Sample size, 10 mm × 10 mm × 0.5 mm to 140 mm × 50 mm × 11 mm
Magazine for 10 samples, alignable *in situ*
Filter for higher-order suppression: Be, C_6H_8, Ti, Cr, Fe, Cu

3. Soft-X-Ray Polarimeter

A. Introduction

In this section we describe the novel high-precision eight-axis UHV polarimeter. It was developed to incorporate a variety of optical elements and was designed and manufactured according to the schematic setup shown in Fig. 9. The main features of the polarimeter are listed in the Table 1. This instrument incorporates two optical elements and thus can be used as a self-calibrating polarization detector or, when either the polarizer or the analyzer is removed, as a versatile reflectometer–ellipsometer. Thus any new kind of optical element can be characterized with respect to its reflection or transmission properties in s- and p-polarization geometry and for transmitting optics with respect to its phase-retarding properties. As many as ten samples of different sizes can be stored in a magazine. From there they can be transferred, mounted, and aligned *in situ* into the measuring position by a wobble-stick mechanism. All positions in the magazine have access to both the polarizer and the analyzer. The device is equipped with UHV-compatible stepper motors and goniometers, which are mounted upon a rigid optical bench. This bench, which is shown in Fig. 10, is prealigned outside the vacuum chamber and is kinematically mounted within the chamber. *In situ* exchangeable pinhole collimators allow for a minimum beam divergence of 2.5 mrad, and higher orders can be suppressed with a set of transmission filters. The chamber was commissioned in November 1997 and is now operational. The individual parts are explained in more detail in what follows.

B. Vacuum Chamber

The chamber is a cylindrical tube with a diameter of 480 mm and a total length of 1200 mm. A base pressure of 1×10^{-6} Pa is achieved with a 520-L/s turbomolecular pump and an oil-free membrane pump. The chamber can be precisely aligned with respect to the incident light axis within an accuracy of ±0.05 mm and ±0.05 mrad. The optical bench inside the chamber is kinematically mounted to decouple temperature-induced distortions of the vacuum chamber from the high precision UHV mechanics. The chamber has two hinged doors on the upstream and the downstream sides through which the optical bench can be removed or installed.

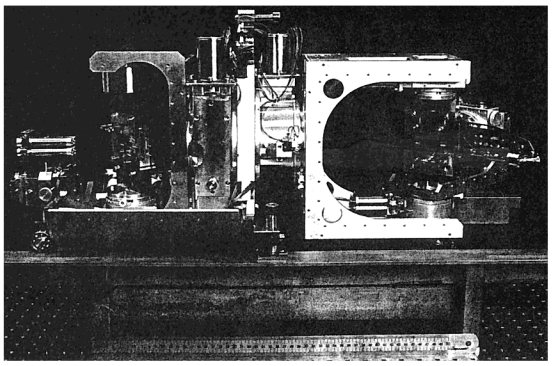

Fig. 10. Photograph of the UHV-compatible optical bench of the polarimeter including collimator, polarizer, analyzer, and detector sections. The incident light comes from the left.

Table 2. Accuracy of Angular Alignment of Optical Axes with Respect To Parallelism (∥) and Perpendicularity (⊥) and of Lateral Alignment with Respect to Parallel Shift (∥) and Intersection (⊥)

Optical Axis		Angular Alignment (°)		Lateral Alignment	
Axis 1	Axis 2	∥	⊥	Shift ∥	Intersection ⊥, (μm)
α	β	0.006	–	50 μm	–
α	θ_P	–	0.0025	–	50
β	θ_A	–	0.002	–	200
β	$2\theta_A$	–	0.006	–	120
θ_A	$2\theta_A$	0.009	–	160 μm	–
$\theta_{P,A}$	Optical surface	0.008	–	≤12 μm	–
Collimator	α	≤0.01	–	Adjustable	–

The 35-kg load of the optical bench arrangement is transported into the chamber on a rail system.

C. Optical Bench

The UHV mechanics of the optical bench consists of four elements: a light collimator, a polarizer, an analyzer, and a detector (see Figs. 9 and 10). All four elements can be moved by UHV-compatible stepper motors so that the whole assembly is an eight-axis polarimeter. The collimator can be translated in the x and y directions perpendicularly to the incident light beam. The polarizer and the analyzer can be rotated independently about the incident light beam (azimuthal angle), and their incidence angles can be set to any angle between normal and grazing incidence. The light detector is scanned in the plane of reflection and off plane. To maintain the alignment of all eight axes, the two translational stages and the six one-circle goniometers are rigidly assembled and aligned upon the optical bench. The technical features of the optical bench, the ranges of angle setting, and the accuracy of all axes are listed in Table 2.

Within the accuracy limit each rotation can be performed without affecting any other angle set previously. The goniometers as well as the translational stages are lubricated with UHV-compatible grease (Fomblin) and driven by UHV-compatible stepper motors, which limit the basic pressure to 1×10^{-6} Pa. All rotation and translation stages of the optical bench were prealigned in the laboratory, and the alignment accuracy was checked with a theodolite and an autocollimator. With the autocollimator the degree to which the angles of all axes were parallel or perpendicular to one another was measured. The theodolite was used to control the lateral displacement of these axes. We confirmed the concentricity of the azimuthal rotation axes (α and β) as well as those of the sample and the detector (θ_A and $2\theta_A$) by using a He–Ne laser beam to check the homogeneity of the transmitted light intensity for a fixed sample detector setting when β was scanned, and similarly for the α axis. In the following subsections we describe the main features of the device, corresponding to Fig. 9, by following the direction of a light beam.

1. *Filter*

A set of absorber filters of different materials (see Table 1), mounted upon a linear feedthrough, can be inserted into the light path to allow for suppression of higher orders in the incident beam in the energy range 55–950 eV.

2. *Collimator*

The divergence of the incoming light can be selected from 2.5 to 25 mrad by a set of four interchangeable pinhole collimators of different sizes, which can be positioned into the beam by the x–y translational stages.

3. *I_0 Detector*

A GaAsP diode or a Au-mesh detector can be moved into the light beam behind the collimator for alignment purposes or for on-line monitoring of the incoming (I_0) intensity.

4. *Polarizer*

The frame holder for the transmission samples is fixed upon a goniometer to define the angle of incidence θ_p. This goniometer is fixed upon a cylinder, which is carried by a second goniometer, allowing for azimuthal rotations α about the incident beam at fixed θ_p. By setting α we can select any sample orientation with respect to the electrical field of the incident radiation, for instance p or s polarization or any other geometry.

5. *Analyzer*

The frame holder for the reflection samples is fixed upon a goniometer to define the angle of incidence θ_A. The detector goniometer for the in-plane angle $2\theta_A$ is mounted upon the opposite side. On this detector arm another goniometer, for the detector off-plane angle θ_D, is fixed. This reflectometer setup is rigidly fixed upon a cylinder, which is mounted upon the β goniometer for azimuthal rotation about the light beam to allow for the realization of p or s polarization or any other geometry. The α and β goniometers that define the optical axis are mounted rigidly back to back upon a base plate to maintain the high precision between these two axes.

6. *Detector*

The detector is a Schottky-type GaAsP photodiode with a sensitive area of 4.6 mm × 4.6 mm and a noise level of 30 fA. It is mounted at normal incidence such as to be insensitive to the polarization characteristics of the light beam. An electrometer is used for readout of the signal. An aperture can be placed in front of the detector to increase the angular resolution to 0.04°. The distance between optical element and detector can be varied to achieve either high angular resolution or large angular acceptance.

7. *Magazine*

A variety of optical elements of different sizes, including multilayers, crystals, mirrors, gratings, and foils,

can be fixed in standard frames for reflection and for transmission samples. As many as ten of these frames can be stored in a magazine inside the chamber. All samples in the magazine have access to both the analyzer and the polarizer. They can be transferred *in situ* to the frame holders of the polarizer and the analyzer by a wobble-stick mechanism (not shown). We can reproducibly position the sample into the measuring position by pushing the sample frame against a kinematic mount within the frame holder. This position is then fixed by a closed-door mechanism. The optical elements are prealigned in the frame holder such that the rotation axes θ_P and θ_A lie upon the appropriate surfaces of the optical elements. The wobble-stick mechanism, however, also allows for *in situ* alignment of the samples with a screwdriver.

D. Computer Control

The polarimeter is completely computer controlled by a 586 PC. For data acquisition, an IEEE 488 interface of the electrometer is used. Additionally, digital or analog signals for data normalization can also be read. The monochromator is connected via a serial interface. The menu-driven software provides the flexibility to perform complex measurement sequences and multidimensional scans listed below.

1. *One-Dimensional Scans*

Scans as functions of photon energy, of time, or of one of the six angles (α, β, θ_P, θ_A, $2\theta_A$, θ_D) can be made while the detector intensity is recorded and displayed. For example, α or β scans permit the azimuthal dependence on the transmission and reflection coefficients to be determined; θ_P or θ_A scans record the transmission or reflection properties as functions of the incidence angle. The data can be normalized simultaneously with respect to the intensity of the incident light, so the reflection coefficient is displayed on line.

2. *Two-Dimensional Scans*

Independent rotation of the polarizer and the analyzer about α and β, respectively (polarimeter scan), enables the Stokes parameters of the incident light and the phase-retarding and polarizing properties of the two optical elements to be determined. With θ_A–$2\theta_A$ scans the reflective properties of multilayers and crystals can be measured.

3. *Three-Dimensional Scans*

The Bragg scan enables a multilayer rocking curve to be followed with energy. At each energy a θ_A–$2\theta_A$ scan is performed. This feature is especially useful for investigations of near-edge absorption structures for which the reflectance changes rapidly.

The grating scan allows the grating efficiency in a certain diffraction order to be followed with energy. While the energy changes, the grating and the detector follow the change automatically according to a constant incidence angle, a constant deviation, or a (plane-grating) fixed-focus mount.

Table 3. Most-Relevant Parameters of Multilayers Investigated in This Paper

System	Period d (nm)	Number of Layer Pairs P	Thickness Ratio $\gamma = d_A/(d_A + d_B)$	Transmission (T) or Reflection (R)
Mo/Si	9.40	100	0.33	R
Mo/Si	9.40	50	0.33	T
Cr/C	3.20	100	0.33	T, R
Cr/Sc	1.57	250	0.66	T, R
Cr/Sc	1.76	200	0.58	T
Cr/Sc	2.04	200	0.49	T
Cr/Sc	2.14	250	0.49	R
Ni/Ti	1.92	75	0.33	R
Ni/Ti	2.33	100	0.33	T

4. Experimental Results

A. Experimental Setup

1. *Monochromator*

The radiation was provided by a 1.5-T bending magnet at the BESSY 800-MeV storage ring, BESSY-I, and by a plane grating Petersen-type (SX700) monochromator, PM 3.[49] The monochromator delivers light with adjustable polarization in the energy range of 30–2000 eV. Vertically movable slits and an adjustable plane mirror in front of the monochromator accept circularly polarized light at offset angles up to $\psi = \pm 0.9$ mrad out of the orbital plane. The in-plane radiation ($\psi = 0$) is linearly polarized. The focus position and the energy calibration of the monochromator are not effected by the selected photon helicity.

The monochromator exit slit was set to 100 μm, providing a resolving power of approximately $E/\Delta E = 1000$. The polarization measurements were performed at a fixed monochromator setting for left-handed circularly polarized light ($\psi = +0.3$ mrad) if not otherwise indicated. The data for Mo/Si were obtained at plane grating monochromator PM 4,[41] providing predominantly linearly polarized synchrotron radiation ($S_1 = 0.85$, $S_2 = 0.05$, and $S_3 = 0.35$ at 95 eV).

2. *Optical Elements*

Cr/C, Cr/Sc, and Ni/Ti multilayers were produced by magnetron sputtering.[38,40–42] The reflection multilayers were grown upon standard Si (100) wafers; the transmission multilayers, upon 120-nm Si_3N_4 support membranes with a window size of 3 mm × 5 mm. Mo/Si was grown by *e*-beam evaporation[50] upon Si (100) wafers and upon 50-nm thin Si_3N_4 membranes with a 2 mm × 2 mm window size. All multilayers were first characterized with monochromatic, unpolarized Cu–K_α radiation emitted from an x-ray tube source. Table 3 lists the most relevant parameters of the reflection and transmission multilayers described in this paper.

B. Reflection Analyzers

The reflective properties of the individual multilayers were described previously.[40–42] In this paper, only

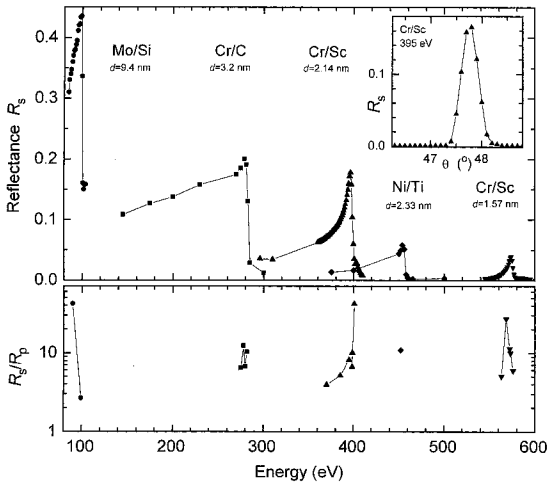

Fig. 11. Experimental survey of multilayer reflection analyzers for the soft-x-ray range. Top, peak reflectance R_s. Each data point was extracted from an energy scan or a θ–2θ-scan, as shown in the inset. Bottom, linear polarizing power of the same multilayers. These data were obtained as fit results from polarization measurements like those shown in Fig. 13 below.

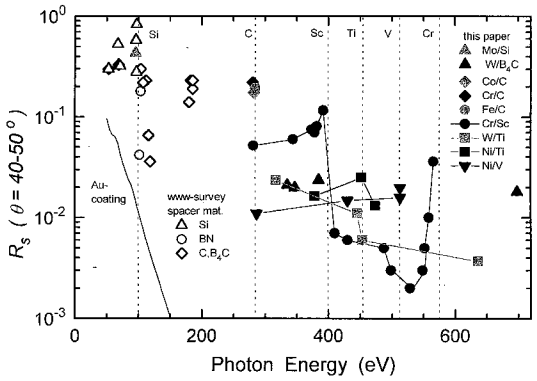

Fig. 12. Multilayers for the soft-x-ray range: Experimental peak reflectance data R_s close to the Brewster's angle. Open symbols, Ref. 51; filled symbols, this paper and Refs. 40–42 and 52.

the results essential for their use in polarimetry applications, namely, reflection and linear polarizing power, are summarized. The multilayers are used as analyzers; i.e., they preferentially reflect only one of the two components of the electrical field (E_s). The suppression of the p component is best done close to the Brewster's angle near 45° (see Subsection 2.B). The measured peak reflectances R_s are plotted in Fig. 11 (top) as function of the photon energy. Each data point was extracted from θ–2θ scans (inset) or from energy scans (not shown) about the Bragg peak. All samples show a strong enhancement of the reflectance at the absorption edges and a sharp cutoff beyond these edges. Period d was chosen such that the multilayers can be operated close to the Brewster's angle at the energy of optimum performance, i.e., the respective absorption edge. The absolute value of R_s is reduced compared with the calculations (Fig. 3) because of the influence of interface roughness.[40–42]

The linear polarizing power R_s/R_p of these samples is shown in Fig. 11 (bottom). Inasmuch as these measurements were made with elliptically polarized light instead of linearly polarized light, the data were extracted from a fit to the polarization measurements (see Subsection 4.C). As expected, the R_s/R_p depends strongly on angle and energy, with a maximum at 45°. The absolute values of R_s/R_p, however, are some orders of magnitude smaller than the calculations shown in Fig. 3. The reasons were reported to be the finite experimental angular and energy resolution of the light beam (Subsection 2.B). Even more essential for this discrepancy is the use of one sample of fixed period in a larger energy–angular range, whereas the calculation was done for an optimum multilayer period matched to each energy at the Brewster's angle.

A summary of all available reflectance data for the soft-x-ray range is given in Fig. 12. Here the reflectance close to the polarizing angle of θ = 45° ± 5° is plotted as function of the photon energy. Each point corresponds to one sample whose d spacing is given by the Bragg equation and the corresponding energy. Open symbols show results taken from the worldwide web survey with spacer materials Si, BN, C, and B_4C.[51] The new multilayers, designed for the water window, are represented by filled symbols. The resonances at the absorption edges of the spacer materials Si, B, C, Sc, Ti, and Cr show up as points of best performance. Although Cr/C delivers more than 20% reflectance at the C 1s edge, with Cr/Sc a reflectance of more than 10% at the Sc 2p edge is achieved. At an energy as high as 700 eV, W/B_4C with a remarkably small d spacing of 1.2 nm gives 1.6% reflectance.

C. Transmission Polarizers

Before their use in polarization experiments, transmission multilayers were systematically investigated with respect to their energy and angular-dependent transmission properties.[40–42] In this paper we present their energy and angular-dependent phase-retarding properties that were obtained with the new polarimeter. Any such measurement consists of eight angular-dependent intensity measurements, i.e., of rotating the polarizer by 360° about the beam axis (angle α) at eight different azimuthal positions of the analyzer (angle β) from 0° to 360°, as in Fig. 2. The angles α = 0° and β = 0° are set to s-polarization geometry.

A typical polarimeter spectrum of the transmitted intensity normalized to the incident intensity is presented in Fig. 13 (symbols) together with curves (solid curves) fitted according to Eq. (8). These spectra were obtained at 397 eV with Cr/Sc as the polarizer (d = 2.04 nm) at θ_P = 46.5° and Cr/Sc as the analyzer (d = 2.14 nm) at θ_A = 47.5°. The two experimental curves, for β (filled symbols) and β + 180° (open symbols), must coincide because of symmetry considerations. Any discrepancy is due to misalignment of the polarimeter axis with respect to the beam axis. A maximum signal is obtained for the analyzer posi-

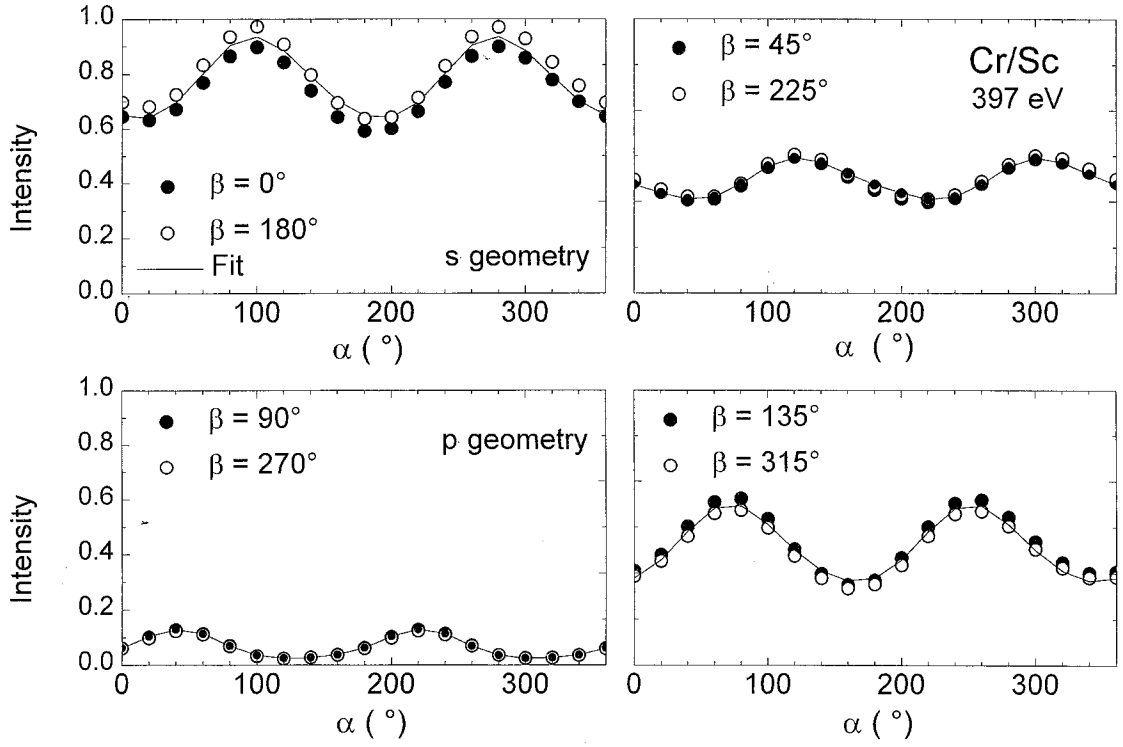

Fig. 13. Polarization measurement with Cr/Sc multilayers at 397 eV (polarimeter scan). Angular distribution of the transmitted intensity as a function of azimuthal polarizer angle α for eight settings of the analyzer azimuth β. Open and filled symbols, experimental data; solid curves, fit results according to Eq. (8), delivering the Stokes parameters of the incident light and the polarizing properties of the two optical elements ($S_0 = 0.98$, $S_1 = 0.9$, $S_2 = 0.05$, $S_3 = 0.38$, $T_p/T_s = 1.2$, $\Delta = -18°$, $R_s/R_p = 10$).

tion $\beta = 0°$, which corresponds to *s*-polarization geometry; $\beta = 90°$ corresponds to *p* geometry. If the polarizer is in *s* geometry, e.g., $\alpha = 0°$, the transmission is minimum, whereas in *p* geometry, $\alpha = 90°$, the transmission is maximum.

A least-squares fit with the CERN software package MINUIT is applied to such a data set, and this yields the characteristics of the light (Stokes vectors $S_0 = 0.98, S_1 = 0.9, S_2 = 0.05$, and $S_3 = 0.38$) as well as the polarization properties of the optics ($T_p/T_s = 1.2$, $\Delta = -18°$, $R_s/R_p = 10$). The relative error was estimated to be approximately 5%. The error is larger (10%) for small Δ, small S_3, or both, because of the correlation of the parameters.

In what follows, the results for the phase retardation Δ and the transmission properties T_s and T_p/T_s obtained according to this procedure are given for all systems investigated. T_s was determined separately.

1. *Cr/Sc*

Figure 14 shows the results obtained for Cr/Sc. A reflection analyzer ($d = 2.14$ nm, $P = 250$) was combined with a nearly identical transmission polarizer ($d = 2.04$ nm, $P = 200$). At three energies close to the Sc 2*p* edge (inset) the phase retardation (Fig. 14, top) was measured as a function of the incidence angle in the vicinity of the Bragg transmission minimum (bottom), where maximum phase retardation was expected. The expected resonance structure is found (top) when the incidence angle is scanned through the Bragg angle. Directly at the edge, the resonant feature is most pronounced, with a maximum phase retardation of $\Delta = -18°$. The angular dependence of Δ is reproduced well by the calculated curves, with roughness ($\sigma = 0.6$ nm) and the angular divergence of the incident light (6.2 mrad) taken into account. The energy resolution was not taken into account. A perfect multilayer ($\sigma = 0$ nm) would deliver $\Delta = -73°$; a λ/4 plate would require 243 periods. The ratio T_p/T_s (Fig. 14, center) reaches a maximum at the Bragg angle, where Δ changes sign (top) and T_s has a minimum (bottom). Above and below the absorption edge the resonance feature fades away.

Figure 15 shows the experimental data for the dependence of the phase retardation on the period of the multilayer. Three Cr/Sc systems with different periods are compared at a fixed energy of 573 eV at the Cr 2*p* edge (inset). The $d = 2.04$ nm sample has a maximum phase retardation of $\Delta = -17°$ at $\theta = 29°$ and has, thus, nearly the same good performance as at the Sc 2*p* edge at a larger incidence angle (see Fig. 14). The $d = 1.76$ nm sample shows a phase retardation of $-11°$; the shortest period multilayer ($d = 1.57$ nm) gives only $\Delta = -7.5°$ at the largest angle of $\theta = 41°$. Good agreement can be achieved between experimental data and calculations (solid curves) when the indicated roughness values are assumed. The results clearly prove the predicted behavior (Subsection 2.C, Fig. 7) of increasing phase retardation

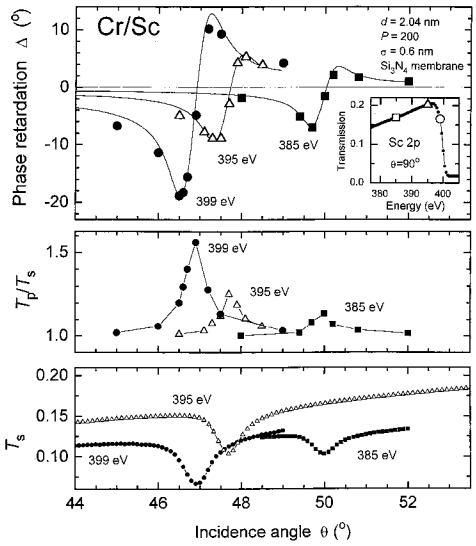

Fig. 14. Polarizing properties of a Cr/Sc transmission multilayer close to the Sc 2*p* edge. Top, phase retardation Δ as function of the incidence angle in the vicinity of the Bragg angle. Each data point was obtained from a polarimeter scan according to Fig. 13. Solid curves, calculation with the assumptions of roughness of σ = 0.6 nm and beam divergence of 6.2 mrad. Inset, normal-incidence transmission (θ = 90). Middle, corresponding transmission ratio T_p/T_s. Bottom, absolute transmission in *s* geometry.

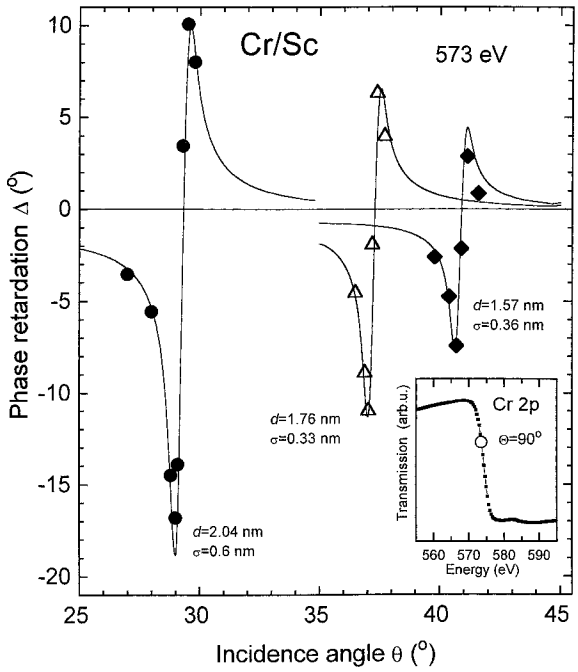

Fig. 15. Polarizing properties of Cr/Sc transmission multilayers close to the Cr 2*p* edge. Angular dependence of the phase retardation on different period thicknesses. Solid curves, calculations including roughness and a beam divergence of 6.2 mrad. The maximum phase retardation increases with decreasing angles of incidence.

with smaller angle of incidence. Thus the d = 2.04 nm sample tailored to work near θ = 30° at the Cr 2*p* edge can be used with a similar performance at both the Sc and the Cr 2*p* edges.

Note that the fitted roughness values are larger than the corresponding data for similar, but reflection-type, multilayers.[41] This result is due to the waviness and roughness of the Si_3N_4 membrane support structure.

2. *Mo/Si*

Figure 16 gives the results for the Mo/Si system (d = 9.4 nm; polarizer, P = 50; analyzer, P = 100). According to the transmission curve (top, inset) the working range of Mo/Si extends from approximately 87 eV to the Si 2*p* edge at 100 eV. The polarizing properties were determined at two energies, 90 and 99.3 eV. The phase retardation (top) and transmission (bottom) were measured as functions of the incidence angle of the polarizer in the vicinity of the Bragg angle. The angular dependence of the phase retardation is reproduced well by the calculated curves with a roughness of σ = 1.6 nm taken into account. A λ/4 (Δ = ±90°) behavior, indicated by dashed lines, is obtained at different angles. A λ/2 plate (Δ = −180°) is also realized at certain angles. For perfect conversion of linearly to circularly polarized light, however, the transmission ratio (Fig. 16, middle) should be close to unity. This condition is fulfilled at small angles away from the resonance, where considerable phase retardation, close to 90°, remains. All data are in good agreement with data published previously.[32,34,35]

3. *Summary*

A survey of the polarizing elements available in the polarimeter for the UV and soft-x-ray ranges is given in Fig. 17. Here the maximum phase retardation measured is plotted as a function of its working energy. The data are extracted from individual results such as those shown in Figs. 14–16. Using a standard MgF_2 optics (8 eV) or Mo/Si, we achieved a λ/4 plate with as much as 100-eV photon energy. The intermediate range can be covered by a triple Au-mirror system.[12] Above 100 eV, roughness and low optical contrast reduce the phase retardation significantly. At the C 1*s* edge a Cr/C system delivers a phase retardation of only −6°. This new result is consistent with previous measurements of a similar system.[33] Ni/Ti has a phase retardation of only −2.2° at 454 eV. This poor behavior was already expected from the reflectance and transmission results.[40,42] This result is obviously due to the small number of periods and the large amount of roughness (σ = 0.75 nm), which were observed and discussed previously.[40,52] The most promising polarizing system is Cr/Sc, which can be used immediately below the 2*p* edges of both Cr and Sc, as discussed with Figs. 14 and 15. The soft-x-ray range can now be covered by four multilayer systems with a performance that is sufficient to permit the degree of polarization to be quantitatively determined to an energy of as much as 575 eV.

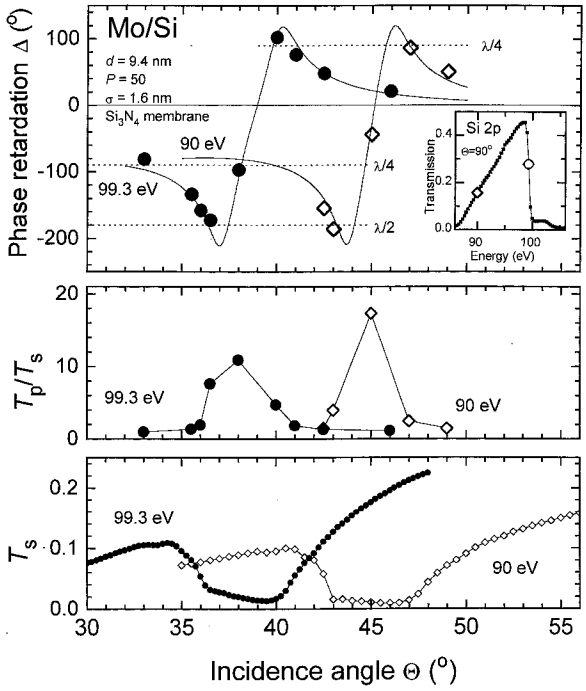

Fig. 16. Polarizing properties of a Mo/Si transmission multilayer close to the Si 2*p* edge. Top, phase retardation Δ as function of the incidence angle in the vicinity of the Bragg angle. Solid curves, calculation assuming a roughness of σ = 1.6 nm and a beam divergence of 6.2 mrad. Inset, normal-incidence transmission (θ = 90). Middle, corresponding transmission ratio T_p/T_s. Bottom, absolute transmission in *s* geometry.

D. Polarization Analysis

Using the newly developed Cr/Sc polarizing system, we could determine the polarization of the BESSY PM 3 circularly polarized beam line at energies of 395 and 573 eV for the first time to our knowledge. The polarization of the monochromatic radiation was measured as a function of the azimuthal angles ψ above and below the electron orbit plane. The Stokes parameters are shown in Fig. 18 (filled symbols, 395 eV; open symbols, 573 eV) together with calculations for 395 eV with the depolarization of the beam-line optics taken into account (solid lines). The error bars of the experimental data are indicated. At the largest azimuthal angles, ψ = ±0.9 mrad, the light is nearly completely circularly polarized: $|S_3| \geq 0.9$. For in-plane radiation (ψ = 0 mrad) the linear polarization is the largest ($S_1 = 0.95$). For light emitted below the orbit plane the S_2-component, which is expected to be zero theoretically, reaches 0.1. S_2 is a measure of the depolarization and misalignment of the beam-line optics. This asymmetry with respect to the orbit plane was found previously.[36]

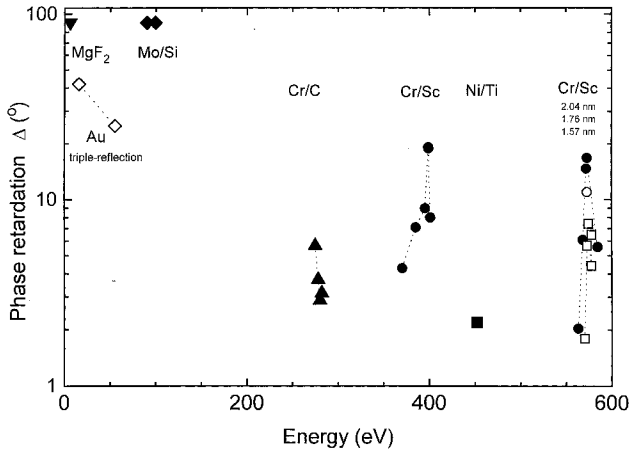

Fig. 17. Polarizers for the soft-x-ray range: survey of experimental phase retardation for a MgF_2 λ/4 plate (8 eV), a triple-reflection polarizer (<100 eV) (Ref. 12), and four transmission multilayers (Figs. 14–16).

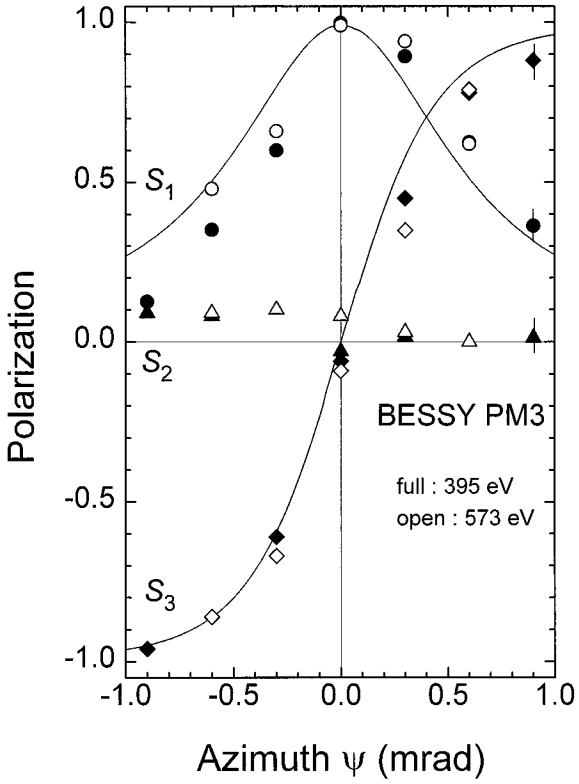

Fig. 18. Linear and circular polarization (Stokes parameters S_1, S_2, and S_3) of the radiation from the BESSY PM 3 monochromator as function of the azimuthal angle ψ for photon energies of 395 and 573 eV measured with Cr/Sc polarimeter optics. Calculations for 395 eV (solid curves).

5. Conclusions

A novel high-precision UHV polarimeter that incorporates a variety of optical elements has been described. This eight-axis polarimeter can be used either as a self-calibrating polarization detector from the visible to the soft-x-ray ranges or, when either the polarizer or the analyzer is removed, as a versatile reflectometer–ellipsometer. Thus any kind of optical element can be characterized with respect to its reflection or transmission properties in *s*- and *p*-polarization geometry and, for transmitting optics, with respect to its polarizing and phase-retarding properties.

Using this polarimeter, we systematically characterized newly developed high-reflectance mirrors and transmission phase retarders, based on multilayer systems, with tunable synchrotron radiation in the soft-x-ray regime. With state-of-the-art Cr/Sc and Ni/Ti multilayers the working range of soft-x-ray polarimetry can be extended beyond the C 1*s* edge to the Cr 2*p* edge at 575 eV. The best performance of the optical elements with respect to reflectance, transmission, and polarizing properties is achieved at and below the 2*p* absorption edges of Si, Sc, Ti, Cr and the 1*s* edge of C, where a maximum phase retardation of as much as $-18°$ (at the Sc and Cr edges) has been determined. By use of a Cr/Sc polarizer–analyzer pair the Stokes parameters of the BESSY circular polarization beam line PM 3 could be determined at energies of as much as 575 eV, yielding a circular polarization of $S_3 = 0.9$.

We plan to use the polarimeter to develop new polarization-sensitive optical elements on the basis of magnetic and nonmagnetic transmission and reflection multilayers and thin films of 3*d* transition metals and rare-earth ions to extend the working range. Based on that approach, a compact detector for online polarization control of synchrotron radiation beam lines will be developed.

This project was supported by the European Community (contract ERBFMGECT 950007). We are indebted to N. N. Salashchenko and E. A. Shamov of the Institute for Physics of Microstructures, Nizhny Novgorod, Russia, for production of the Cr/Sc multilayers. We are grateful to H. Grimmer, D. Clemens, P. Böni, and M. Horisberger of the Paul Scherrer Institut, Villigen, Switzerland, for the Ni/Ti samples. E. Louis, E. Maas, and F. Bijkerk of the Institute for Plasma Physics Rijnhuizen Laser Plasma and X-ray Optics, Rijnhuizen, the Netherlands, produced the Mo/Si multilayer. The W/B_4C multilayer was produced by Y. Platonov of Osmic Inc., USA. The Si_3N_4 membranes were manufactured by B. Löchel of the Institute for Si-Technology, Berlin. Ch. Jung and G. Reichardt of BESSY are thanked for valuable comments on the manuscript.

References

1. J. Bahrdt, A. Gaupp, W. Gudat, M. Mast, K. Molter, W. B. Peatman, M. Scheer, Th. Schroeter, and Ch. Wang, "Circular polarized synchrotron radiation from the crossed undulator at BESSY," Rev. Sci. Instrum. **63,** 339–342 (1992).
2. R. P. Walker and B. Diviacco, "Studies of insertion devices for producing circularly polarized radiation with variable helicity in ELETTRA," Rev. Sci. Instrum. **63,** 332–335 (1992).
3. R. Carr, J. B. Kortright, M. Rice, and S. Lidia, "Performance of the elliptically polarizing undulator on SPEAR," Rev. Sci. Instrum. **66,** 1862–1864 (1995).
4. K. J. S. Sawhney, F. Senf, M. Scheer, F. Schäfers, J. Bahrdt, A. Gaupp, and W. Gudat, "A novel undulator-based PGM beamline for circularly polarized synchrotron radiation at BESSY II," Nucl. Instrum. Meth. A **390,** 395–402 (1997).
5. F. M. F. de Groot, "X-ray absorption and dichroism of transition metals and their compounds," J. Electron. Spectrosc. Related Phenom. **67,** 529–622 (1994).
6. J. B. Goedkoop, B. T. Thole, G. van der Laan, G. A. Sawatzky, F. M. F. de Groot, and J. C. Fuggle, "Calculations of magnetic x-ray dichroism in the 3*d* absorption spectra of rare earth compounds," Phys. Rev. B **37,** 2086–2093 (1988).
7. U. Heinzmann and N. A. Cherepkov, "Spin polarization in photoionization," *VUV and Soft X-Ray Photoionization Studies*, U. Becker and D. A. Shirley, eds., (Plenum, New York, 1996), pp. 512–529.
8. P. Fischer, G. Schütz, G. Schmahl, P. Guttmann, and D. Rasch, "Imaging of magnetic domains with the x-ray microscope at BESSY using X-ray magnetic circular dichroism," Z. Phys. B **101,** 313–316 (1996).
9. Y. Petroff, "Neutron beams and synchrotron radiation sources," presented at Mega Science, The OECD Forum, Organization for Economonic Cooperation and Development, Paris, 1994.
10. G. Schönhense, "Circular dichroism and spin polarization in photoemission from adsorbates and nonmagnetic solids," Phys. Scr. **T31,** 255–275 (1990).
11. D. S. Kliger, J. W. Lewis, and C. E. Randall, *Polarized Light in Optics and Spectroscopy* (Academic, San Diego, Calif., 1990).
12. A. Gaupp and M. Mast, "First experimental experience with a VUV polarimeter at BESSY," Rev. Sci. Instrum. **60,** 2213–2215 (1989).
13. W. B. Westerveld, K. Becker, P. W. Zetner, J. J. Corr, and J. W. McConkey, "Production and measurement of circular polarization in the VUV," Appl. Opt. **24,** 2256–2262 (1985).
14. P. A. Williams, A. H. Rose, and C. M. Wang, "Rotating-polarizer polarimeter for accurate retardance measurement," Appl. Opt. **36,** 6466–6472 (1997).
15. D. E. Aspnes and A. A. Studna, "High-precision scanning ellipsometer," Appl. Opt. **14,** 220–228 (1975).
16. T. Koide, T. Shidara, M. Yuri, N. Kadaka, K. Yamaguchi, and H. Fukutani, "Elliptical-polarization analysis of synchrotron radiation in the 5–80 eV region with a reflection polarimeter," Nucl. Instrum. Methods A **308,** 635–644 (1991).
17. A. Gaupp and W. Peatman, "A polarimeter for soft x-rays," in *Soft X-Ray Optics and Technology*, E. E. Koch and G. A. Schmahl, eds., Proc. SPIE **733,** 272–273 (1986).
18. P. Dhez, "Polarizers and polarimeters in the x–uv range," Nucl. Instrum. Methods A **261,** 66–71 (1987).
19. W. R. Hunter, "Polarizers for the extreme ultraviolet," Jpn. J. Appl. Phys. **4,** Suppl. 1, 520–526 (1965).
20. E. Spiller, "Multilayer interference coatings for the vacuum ultraviolet," in *Space Optics*, B. J. Thompson and R. R. Shannon, eds. (National Academy of Sciences, Washington, D. C., 1974), pp. 581–597.
21. K. Rabinovitch, L. R. Canfield, and R. P. Madden, "A method for measuring polarization in the vacuum ultraviolet," Appl. Opt. **4,** 1005–1010 (1965).
22. E. S. Gluskin, S. V. Gaponov, P. Dhez, P. P. Ilyinsky, N. N. Salashchenko, Y. M. Shatunov, and E. M. Trakhtenberg, "A polarimeter for soft x-ray and VUV radiation," Nucl. Instrum. Methods A **246,** 394–396 (1986).
23. N. B. Baranova and B. Y. Zeldovich, "Birefringence and gyrotropoy due to nearly Bragglike processes in the x-ray region," Sov. Phys. JETP **52,** 900–904 (1980).
24. J. A. Golovchenko, B. M. Kincaid, R. A. Levesque, A. E. Meixner, and D. R. Kaplan, "Polarization pendellösung and the generation of circularly polarized x-rays with a quarter wave plate," Phys. Rev. Lett. **57,** 202–205 (1986).
25. D. M. Mills, "Spin-aligned momentum distributions of transition-metal ferromagnets studied with circularly polarized synchrotron radiation," Phys. Rev. B **36,** 6178–6181 (1987).
26. J. C. Lang and G. Strajer, "Bragg transmission phase plates for the production of circularly polarized x-rays," Rev. Sci. Instrum. **66,** 1540–1542 (1995).
27. A. Kaprolat, K.-J. Gabriel, W. Schülke, P. Fischer, and G. Schütz, "Si Bragg-case transmission phase plate used for the

production of circular polarized synchrotron radiation," Nucl. Instrum. Methods A **361,** 358–363 (1995).
28. K. Holldack, F. Schäfers, T. Kachel, and I. Packe, "A detector for circular polarization of soft x-rays," Rev. Sci. Instrum. **67,** 2485–2489 (1996).
29. J. B. Kortright, B. Rice, and R. Carr, "Soft x-ray Faraday rotation at Fe $L_{2,3}$ edges," Phys. Rev. B **51,** 10,240–10,243 (1995).
30. J. B. Kortright and J. H. Underwood, "Multilayer optical elements for generation and analysis of circularly polarized x-rays," Nucl. Instrum. Methods A **291,** 272–277 (1990).
31. J. B. Kortright, "Polarization properties of multilayers in the EUV and soft x-ray," in *X-Ray and Ultraviolet Polarimetry*, S. Fineschi, ed., Proc. SPIE **2010,** 160–167 (1993).
32. J. B. Kortright, H. Kimura, V. Nikitin, K. Mayama, M. Yamamoto, and M. Yanagihara, "Soft x-ray (97 eV) phase retardation using transmission multilayers," Appl. Phys. Lett. **60,** 2963–2965 (1992).
33. H. Kimura, T. Miyahara, Y. Goto, K. Mayama, M. Yanagihara, and M. Yamamoto, "Polarisation measurement of SR from a helical undulator using a quarter-wave plate for a wavelength of 12.8 nm," Rev. Sci. Instrum. **66,** 1920–1922 (1995).
34. H. Kimura, M. Yamamoto, M. Yanagihara, T. Maehara, and T. Namioka, "Full polarization measurement of synchrotron radiation with use of soft x-ray multilayers," Rev. Sci. Instrum. **63,** 1379–1382 (1992).
35. J. Viefhaus, L. Avaldi, G. Snell, M. Wiedenhöft, R. Hentges, A. Rüdel, F. Schäfers, D. Menke, U. Heinzmann, A. Engelns, J. Berakdar, H. Klar, and U. Becker, "Experimental evidence for circular dichroism in the double photoionization of helium," Phys. Rev. Lett. **19,** 3975–3978 (1996).
36. S. Di Fonzo, W. Jark, F. Schäfers, H. Petersen, A. Gaupp, and J. H. Underwood, "Phase retardation and full polarization analysis of soft-x-ray synchrotron radiation close to the carbon K edge by use of a multilayer transmission filter," Appl. Opt. **33,** 2624–2632 (1994).
37. F. Schäfers, H. Petersen, A. Gaupp, S. DiFonzo, W. Jark, and J. H. Underwood, "Measurement of circular polarization close to the carbon K-edge using a transmission multilayer," in *X-Ray and Ultraviolet Polarimetry*, S. Fineschi, ed., Proc. SPIE **2010,** 57–59 (1993).
38. S. DiFonzo, R. Müller, W. Jark, A. Gaupp, F. Schäfers, and J. H. Underwood, "Multilayer transmission phase shifters for the carbon K edge and the water window," Rev. Sci. Instrum. **66,** 1513–1516 (1995).
39. C. Montcalm, P. A. Kearney, J. M. Slaughter, B. T. Sullivan, M. Chaker, H. Pepin, and C. M. Falco, "Survey of Ti-, B-, and Y-based soft x-ray–extreme ultraviolet multilayer mirrors for the 2- to 12-nm wavelength region," Appl. Opt. **35,** 5134–5147 (1996).
40. H.-Ch. Mertins, F. Schäfers, H. Grimmer, P. Böni, and M. Horrisberger, "W/C, W/Ti, Ni/Ti and Ni/V multilayers for the soft-x-ray range: experimental investigation with synchrotron radiation," Appl. Opt. **37,** 1873–1882 (1998).
41. F. Schäfers, H.-Ch. Mertins, F. Schmolla, I. Packe, N. N. Salashchenko, and E. A. Shamov, "Cr/Sc multilayers for the soft-x-ray range," Appl. Opt. **37,** 719–728 (1998).
42. F. Schäfers, H.-Ch. Mertins, M. Mertin, I. Packe, F. Schmolla, S. Di Fonzo, G. Soullie, W. Jark, H. Grimmer, P. Böeni, D. Clemens, M. Horisberger, N. N. Salashchenko, and E. A. Shamov, "Experimental multilayer survey in the VUV," in *Materials, Manufacturing and Measurement for Synchrotron Radiation Mirrors*, P. Z. Takacs and T. W. Tonnessen, eds., Proc. SPIE **3152,** 222–230 (1997).
43. J. B. Kortright, M. Rice, and K. D. Franck, "Tunable multilayer EUV/soft x-ray polarimeter," Rev. Sci. Instrum. **66,** 1567–1569 (1995).
44. R. L. Johnson, J. Barth, and M. Cardona, "Spectroscopic ellipsometry with synchrotron radiation," Rev. Sci. Instrum. **60,** 2209–2212 (1989).
45. F. Schäfers and M. Krumrey, "REFLEC—a program to calculate soft x-ray optical elements and synchrotron radiation beamlines," Tech. Rep. BESSY TB 201 (Berliner Elektronenspeicherring-Gesellschaft für Synchrotronstrahlung mbH, Berlin, 1996).
46. B. L. Henke, E. M. Gullikson, and J. C. Davis, "X-ray interactions: photoabsorption, scattering, transmission and reflection at E = 50–30000 eV, Z = 1–92," At. Data Nucl. Data Tables **54,** 181–342 (1993).
47. J. B. Kortright and A. Fischer-Colbrie, "Standing wave enhanced scattering in multilayer structures," J. Appl. Phys. **61,** 1130–1133 (1987).
48. V. Sh. Machavariani, "Quarter wave plate in near edge soft x-ray region based on the total external reflection principle," Phys. Rev. Lett. **80,** 1541–1543 (1998).
49. H. Petersen, M. Willmann, F. Schäfers, and W. Gudat, "Circularly polarized soft x-rays in the photon energy range 30–2000 eV at the BESSY SX700/3," Nucl. Instrum. Methods A **333,** 594–598 (1993).
50. H.-J. Voorma, E. Louis, F. Bijkerk, and S. Abdali, "Angular and energy dependence of ion bombardment of Mo/Si multilayers," J. Appl. Phys. **82,** 1876–1881 (1997).
51. For further information see http://www-cxro.lblgov/multilayer/survey.html.
52. H. Grimmer, M. Horrisberger, U. Staub, H.-Ch. Mertins, and F. Schäfers, "Multilayer optics for soft x-rays," Bull. Czech Slov. Crystallogr. Assoc. (to be published).
53. M. Maaza, B. Farnoux, F. Samuel, C. Sella, F. Wehling, F. Bridou, M. Groos, B. Pardo, and G. Foulet, "Reduction of the interfacial diffusion in Ni–Ti neutron optics multilayers by carburation of the Ni–Ti interfaces," J. Appl. Crystallogr. **26,** 574–582 (1993).